PERGAMON

International Journal of Heat and Mass Transfer 46 (2003) 671–685

International Journal of HEAT and MASS TRANSFER

www.elsevier.com/locate/ijhmt

Startup of a horizontal lithium–molybdenum heat pipe from a frozen state

Jean-Michel Tournier, Mohamed S. El-Genk *

Institute for Space and Nuclear Power Studies, Department of Chemical and Nuclear Engineering, School of Engineering, The University of New Mexico, Albuquerque, NM 87131, USA

Received 3 August 2001; received in revised form 3 August 2002

Abstract

Results of the simulation of the startup from a frozen state of a molybdenum heat pipe with lithium working fluid are presented and discussed. The 1.8-m-long heat pipe was tested in the horizontal position and had a liquid annular space between the porous wick and the wall. The 30-cm-long evaporator section was inductively heated and the 147-cm-long condenser was cooled by thermal radiation to the quartz tube enclosing the heat pipe and to the ambient. The space between the quartz tube and the heat pipe was evacuated in order to minimize heat losses by convection and conduction. Model results on the progression of the thaw front, liquid pooling at the end of the condenser, and the wall temperature along the heat pipe were found to be in good agreement with experimental measurements. Results showed that, as the heat pipe reached quasi-steady state operation at an evaporator wall temperature of 1550 K, the wall temperature near the end of the condenser dropped precipitously by 450 K, because of the formation of a 8.3-cm-long liquid plug and the end heat losses in the condenser.

1. Introduction

For high temperature applications requiring transport of large amounts of thermal power from a compact heat source, such as a nuclear reactor, at a small temperature difference between the heat source and the heat sink, liquid metal heat pipes are a prime choice. Other applications of such devices include lightweight heat rejection radiator for space power systems and thermal-photovoltaic direct energy conversion systems. For such applications, alkali-metal heat pipes offer high redundancy for heat removal at high heat fluxes and a wide range of source temperatures above 700 K. The latter dictates the choice of working fluid, in order of increasing temperature, potassium, sodium, and lithium. Power throughputs as high as 15 and 30 kW/cm^2 are possible with sodium and lithium heat pipes, respectively, at 1150 and 1580 K, respectively. Above 1200 K, lithium is the best choice for a working fluid, because of its low vapor pressure, high figure-of-merit, and high latent heat of vaporization and surface tension. A concern with using liquid metal working fluids in heat pipes, and in particular lithium, is that they are typically frozen at startup. Lithium has a relatively high melting point of 453.7 K, at which its vapor pressure is extremely low (~0.1 μPa). Therefore, the following issues are worthy of investigating, namely: (a) how long does the full thaw of a lithium heat pipe take? (b) will the heat pipe experience a dryout in the evaporator wick during the startup from a frozen state? and (c) since the lithium working fluid experiences a volume increase well in excess of 20% as it thaws and heats up to operating temperature, where does the excess liquid go and how does it affect the operation of the heat pipe?

At the startup of a lithium heat pipe, the vapor pressure is typically on the order of nPa, at which the mean-free-path of the vapor molecules is large compared to the diameter of the vapor core, hence the vapor flow in the evaporator is in the free-molecular flow regime [1]. After the working fluid in the evaporator section melts, the vapor pressure increases, and the vapor flow becomes in the transition regime. Eventually, the vapor

* Corresponding author. Tel.: +1-505-277-5442; fax: +1-505-277-2814.

E-mail address: mgenk@unm.edu (M.S. El-Genk).

0017-9310/03/$ - see front matter
PII: S0017-9310(02)00324-1

Nomenclature

a_{cc}	accommodation coefficient
A	surface area (m^2)
C_1	first radiation constant, 3.7415×10^{-16} m^2 W
C_2	second radiation constant, 1.4388×10^{-2} m K
G	average flow mass flux (kg/m^2 s)
G'	fraction of blackbody emittance
K	wick permeability (m^2)
k	Boltzmann constant, $k = 1.3804 \times 10^{-23}$ J/K
M	molecular weight of working fluid (kg/mol)
M_λ	spectral radiance per unit wavelength (W/m^2 m)
$\dot{\bar{m}}$	evaporation/condensation/sublimation/resolidification mass flux (kg/m^2 s)
$\dot{m}^{POOL}$	pooling rate (kg/s)
M_{POOL}	mass of liquid pool in vapor core (kg)
N	number of axial sections along wall
N_{mush}	axial location of thaw front
N_{wet}	axial location of first wet point
N_z	number of axial sections along wick
P	pressure (Pa)
q_0^{out}	outgoing radiant flux from quartz tube (W/m^2)
Q^{loss}	net radiant heat loss (W)
R_c	radius of curvature of interfacial liquid meniscus (m)
R_g	universal gas constant, $R_g = 8.3143$ J/mol K
R_{int}	radius of L–V interface (m)
R_p	wick effective pore radius (m)
R_v	radius of vapor core (m)
t	time (s)
T	temperature (K)
T_{fus}	fluid fusion temperature (K)
T_{int}	L–V interface temperature (K)
T_{tr}	transition temperature between vapor flow regimes (K)
T_R	ambient temperature (K)
Vol	volume of numerical cell (m^3)
V_p	volume of hemispherical pores at wick surface (m^3)
WET_j	flag for interfacial condition

Greek symbols

β	dimensionless coefficient, $C_2/(\lambda_c T)$
α_p	void fraction in interfacial wick pores
γ	volume fraction of frozen fluid
δ_{kp}	Kronecker delta, $\delta_{kk} = 1$, $\delta_{kp} = 0$ if $k \neq p$
ΔR_i	size of radial computation cell (m)
Δt	discretization time step (s)
ΔZ_j	size of axial computation cell (m)
ε	volume porosity of porous wick
ε_k	hemispherical emissivity of surface A_k
ε_λ	spectral emittance of quartz
$\bar{\varepsilon}_0$	effective emissivity of quartz
θ_w	liquid/wick wetting angle (radian)
λ	radiation wavelength (m)
λ_c	cut-off wavelength (m)
μ_c	cosine of contact angle of liquid meniscus at L–V interface, R_p/R_c
ρ	density (kg/m^3)
λ	spectral reflectance of quartz
σ	Stefan–Boltzmann constant, 5.67×10^{-8} W/m^2 K^4
σ^L	liquid surface tension (N/m)
τ_λ	spectral transmittance of quartz
$\bar{\tau}_0$	effective transmittivity of quartz

Subscript/superscript

i	radial cell number
j	axial cell number
L	liquid phase
n	temporal discretization number
o	quartz tube inner surface
r	radial component
R	room/ambient
sat	saturation
V	vapor phase
z	axial component
*	best estimate at new time
′	correction

flow transitions to the continuum flow regime as the heat pipe temperature reaches hundreds of degrees Kelvin above the fusion temperature of lithium. In the continuum flow regime, which is characterized by a very small mean-free-path compared to the vapor core diameter, the momentum transfer of the working fluid is dominated by the molecule–molecule collisions. In the intermediate transition flow regime, the effects of both molecule–molecule and molecule–wall collisions are important [1]. Owing to the very low vapor transport in the molecular and the transition flow regimes, the startup of a lithium heat pipe from a frozen state could take several hours. To speed up such startup, the heat pipe is partially charged with a non-condensable inert gas such as argon or helium [2,3], whose effect is outside the scope of this paper.

When simulating the startup of a liquid metal heat pipe from a frozen state, in addition to dealing with the

transitions in the vapor flow, it is important to accurately predict the transient progression of the thaw front in the wick structure and in the surrounding annulus, if any, as well as account for the working fluid's volume increase as it melts and heats up in temperature. Due to the very low vapor pressure of lithium, the vapor flow does not transition to the viscous (or continuum) flow regime until the heat pipe temperature is relatively high [1]. Up to 800 K, the lithium vapor flow is typically in the molecular regime ($\sim$1 Pa), in the transition flow regime between 800 and 1050 K ($\sim$1–250 Pa), and in the viscous regime above 1050 K (>250 Pa) [1]. These flow regimes affect the thermal response of the heat pipe during the startup for a frozen state, and should be modeled accurately to allow for a smooth transition between successive regimes. These vapor flow regimes could all co-exist in the vapor core, and should be tracked with time during the startup transient. Such complexities of the startup from a frozen state require the development and implementation of efficient and sophisticated numerical schemes for solving the coupled governing equations in the vapor, wall, wick, and the annular space, and for tracking not only the thaw front, but also the progression of the various vapor flow regimes in the heat pipe. In addition, special attention must be given to predicting the location as well as the movement of the wet point forming at the vapor–wick interface (where the liquid meniscus in the surface pores of the wick is flat), and accounting for the pooling of the excess liquid in the vapor core at the end of the condenser.

A few models have been developed to simulate the startup of alkali-metal heat pipes from a frozen state. Jang et al. [4] have developed a pure-conduction heat capacity model to track the thaw process in the wick, and modeled the vapor flow using a one-dimensional transient compressible flow model. The transition temperature at a Knudsen number of 0.01 was used to indicate the location of the free-molecule flow front, and the heat and mass transfer at the boundaries of the rarefied vapor zone was neglected. Cao and Faghri [5,6] improved the model of Jang et al. [4] by implementing a fixed-grid enthalpy method to handle the thaw in the wick, and modeling the continuum vapor flow regime as a two-dimensional compressible flow. They described the rarefied vapor flow regime using a self-diffusion model, and coupled it to the continuum vapor flow region with appropriate boundary conditions at the transition front defined by the transition temperature. Cao and Faghri [5] have successfully predicted the axial wall temperature distribution in a sodium heat pipe tested at Wright State University, but calculated vapor Mach numbers as high as six during the startup from a frozen state [5].

The Thermal Hydraulic Response Of Heat Pipes Under Transients code of Hall et al. [7,8] incorporates the liquid flow in the wick, hydrodynamically couples the liquid and vapor phases, describes the various vapor flow regimes using the dusty gas model, and accounts for the effect of a non-condensable gas (air) in the heat pipe. The two-dimensional conservation equations were averaged over the radial direction, yielding basically one-dimensional vapor and wick models, and the melting in the wick was described using an approximate solution. In an unsuccessful attempt to reproduce the experimental results of the SPAR-8 lithium heat pipe [9], Hall and Doster [7] varied the values of the evaporation and condensation accommodation coefficients used in the code. In a later version of the code, Hall et al. [8] allowed a negative liquid pressure (tension) to develop in the wick, and used an accommodation coefficient of unity to calculate the evaporation and condensation rates. With these modifications, the code's predictions of the experimental data of the SPAR-8 lithium heat pipe startup were greatly improved. However, the predicted temperatures lagged behind measurements at latter times, suggesting that the net heat input to the evaporator used in the code was lower than the actual value in the experiment [8].

The Heat Pipe Transient Analysis Model (HPTAM), developed at the University of New Mexico's Institute for Space and Nuclear Power Studies [10–12], attempted to avoid some of the limitations of previous codes and thoroughly model the vapor flow transitions and progression of the thaw front, including the formation of the "wet point" and of a pool of excess liquid at the end of the condenser. A two-dimensional, homogeneous enthalpy method, in conjunction with the extended Darcy's continuity and momentum equations [10] is used to model the phase change of the working fluid and liquid flow in the wick. The liquid and vapor phases are hydrodynamically coupled, allowing tension to develop in the liquid phase. The Dusty Gas Model is used to describe the free-molecule, transition, and continuum vapor flow regimes [11]. In addition, an efficient numerical technique is used to solve the coupled governing equations in the wall, wick and vapor regions [12].

The predictions of HPTAM have been in good agreement with experimental data for the startup of a sodium heat pipe from a frozen state [11,13]. Very little data have been reported for the startup of lithium heat pipes from a frozen state. However, recently [14], experiments have been carried out at Los Alamos National Laboratory (LANL), using a 1.8-m-long lithium/molybdenum (Li/Mo) heat pipe with an annular space, to determine the duration of the startup transient to steady-state operation at $\sim$1500 K, track the progression of the thaw front and the accumulation of excess liquid at the end of the condenser as function of time, and study the thermal response of the heat pipe during startup from a frozen state as a function of inclination angle [14].

The objective of this work was to simulate the startup transient of the lithium–molybdenum heat pipe tested recently in the horizontal position at LANL, subjected to a ramped power input, and compare the model's results with experimental measurements [14]. In order to simulate such a startup experiment, additional capabilities have been added to HPTAM, such as modeling the mass, momentum, and heat transfers in the annular space between the porous wick and the heat pipe wall, simulating radiation heat exchange between the pipe wall, the surrounding semi-transparent quartz tube and the room, and predicting the accumulation of excess liquid in the vapor core and at the end of the condenser during the startup transient. Some of these new capabilities are described in this paper and the procedure used to estimate the net thermal power input to the inductively heated evaporator section in the experiment is detailed. Finally, the predictions of the startup transient of the horizontal Li/Mo heat pipe from a frozen state are compared with the reported measurements of the wall temperatures, the thaw front location, and the extent of the liquid plug at the end of the condenser.

2. Lithium/molybdenum heat pipe

A schematic of the lithium heat pipe is shown in Fig. 1. The heat pipe has a free-floating, Mo–41wt.%Re 400-mesh screen wick (0.41-mm-thick), and a 1.52-mm-thick, molybdenum wall. The heat pipe is 1.8-m-long and 19.1 mm O.D. A 0.37 mm annular gap separates the wick from the wall. The evaporator end of the wick is closed with a fitted Mo plug (12.7-mm-long cylinder), retained mechanically with a Mo wire wrap, and brazed in place with a Zr filler material [14]. The plug attachment piece (not shown in Fig. 1) is a small Mo cylinder 6.35 mm in length and 3.175 mm in diameter. The evaporator end plug of the heat pipe is a 6.35-mm-long piece of molybdenum. The 10.95-mm-long section between the evaporator end plug and the wick plug opens to the liquid annulus (Fig. 1) and contains an oxygen-getter pack of 20, 0.125-mm-thick, hafnium foils. The foils are dimpled to provide a liquid flow path and are strung together on a Mo wire. The lithium charge in the heat pipe is estimated at 30 g. The Mo–41wt.%Re wick is comprised of 7 layers of a 400-mesh woven screen of 25-μm diameter wires. The wick is 0.41-mm-thick, and has a volume porosity, $\varepsilon = 0.7093$, permeability, $K = 2.167 \times 10^{-11}$ m^2, and effective pore radius $R_p = 19.3$ μm [10,14]. The insert in Fig. 1 shows a schematic of the heat pipe test setup. As shown in the insert, the lithium heat pipe was enclosed into a semi-transparent, evacuated quartz tube. The induction coil was placed around the quartz tube, along the evaporator section of the heat pipe. In the experiment, the molybdenum pipe lost heat from the wall by radiation to the quartz tube and the surroundings. Therefore, the first step in modeling the startup of the lithium heat pipe shown in Fig. 1 was to determine the net power input to the evaporator section of the heat pipe in the experiment, after accounting for the radiation heat losses.

3. Model description

The heat pipe is divided into four radial regions: wall, annular space, wick, and vapor core (Fig. 1). During thaw, the liquid and frozen volume fractions of the working fluid in the annulus and the wick regions are calculated as functions of time, taking into account the increase in the lithium volume with thaw and heat-up to steady-state operation temperature of 1500 K. The volume of the excess liquid, its relocation, and eventual accumulation at the end of the condenser section in the vapor core of the heat pipe, are determined. In addition, the spatial and temporal temperature distributions in the wall, and the temperatures, pressures, and mass fluxes of the liquid (L) and the vapor (V) along the heat pipe are calculated. Finally, through thermal and hydrodynamic couplings of the liquid and vapor phases, the local radius of curvature of the liquid meniscus in the surfaces pores of the wick is calculated.

The transient form of the pure-conduction equation in the wall is solved for the wall temperature, and the extended Darcy's equations are solved for the liquid flow in the porous wick [10]. To track the thaw front in the wick and the surrounding annulus, the volume-averaged, homogeneous enthalpy equations in these regions are solved for the local frozen volume fractions and temperatures as functions of time [10]. The solution uses a fixed-grid technique, for which implicit tracking of the liquid–solid interface within the wick is not necessary. The wick permeability is calculated in terms of the volume fraction of the melt, which ensures that the permeability and the melt velocity approach zero in the frozen region. The density of the liquid in the wick and the surrounding annulus is calculated as a function of pressure and temperature to account for the thermal expansion of the working fluid. The free-molecule, transition and continuum flow regimes in the vapor core of the heat pipe are modeled using the dusty-gas-model [1,11]. The sublimation, evaporation, condensation, and re-solidification rates of the working fluid during the startup transient are calculated as functions of time and location, using the kinetic theory of gases, with an accommodation coefficient of unity [10].

The governing equations in the four regions of the Li/Mo heat pipe (vapor, wick, annulus, and wall) are solved subject to appropriate boundary and initial conditions: (a) zero liquid velocity at all solid boundaries; (b) evaporator end is adiabatic; (c) radiative boundary at the outer wall surface along the heat pipe; (d) at the

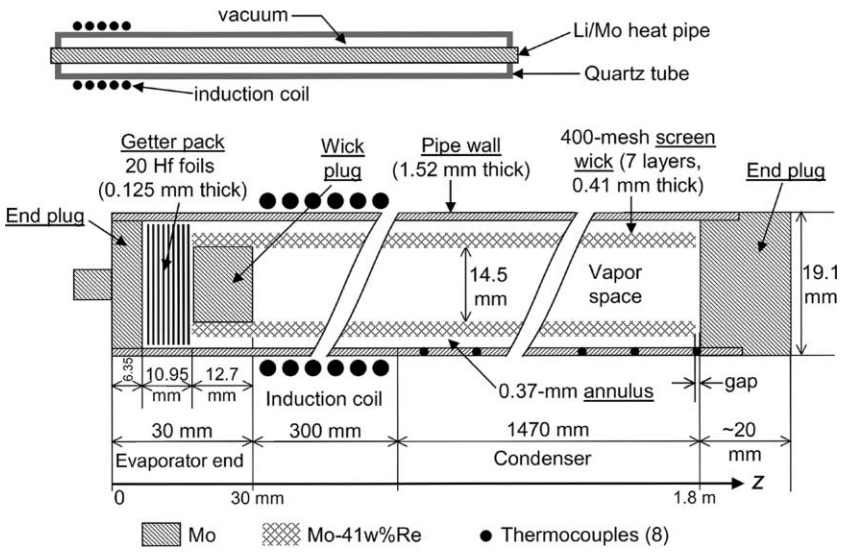

Fig. 1. Cutaway view of 1.8-m-long molybdenum–lithium heat pipe (not to scale).

beginning of the startup from a frozen state, the temperatures of the vapor, frozen fluid, and wall are uniform and equal; and (e) the vapor temperature changes with time during the startup transient, but is always at saturation. The solution of the non-linear governing equations and the thermal and hydrodynamic couplings between the liquid, solid, and vapor phases of the working fluid is handled using a stable numerical technique [12].

The additional modeling capabilities developed to simulate the frozen startup of the lithium heat pipe [14] (Fig. 1) include: (a) tracking the movement of the excess liquid and eventual accumulation at the end of the condenser; (b) solving the mass, momentum, and energy balance equations in the annular gap between the wick and the heat pipe wall, subjected to interfacial boundary conditions with the wick and the wall regions; (c) solving the transient, two-dimensional heat conduction equation for the condenser end plug, which is radiatively cooled on the outside (Fig. 1); and (d) incorporating a two-waveband approximation model to describe the radiation characteristics of the quartz tube surrounding the heat pipe, and calculate the radiation heat losses along the length of the heat pipe, for accurately determining the thermal power input to the evaporator section in the experiment [14]. Some of these additional modeling capabilities are described next.

3.1. Vapor–wick interfacial model and liquid pooling in vapor core

A two-dimensional, staggered grid [10,12], in cylindrical coordinates, is used to solve the governing equations in the vapor, wick, annular gap, and the wall regions. The dimensions of the numerical cell (i, j) are ΔR_i and ΔZ_j, and the side surface areas of the cell (i, j) are $A_r^{i,j}$, $A_r^{i-1,j}$, $A_z^{i,j}$ and $A_z^{i,j-1}$, in the radial and axial directions, respectively. Densities, pressures, temperatures and enthalpies are calculated at the center of mass cells, while the velocities and mass fluxes are determined at the centers of the faces of the cells. The superscripts (n) and $(n+1)$ refer to the variables at the present and new time steps, respectively, while the superscript (*) refers to the best estimate of the new-time variable at the computation time. Given a best estimate of a new-time quantity, for example the pressure (P^*), the numerical solution seeks a primed correction field (P') such that: $P^{n+1} = P^* + P'$. The time discretization is fully implicit, providing a robust numerical solution and allowing the use of reasonable time steps. The mass balance equation in the computation cell (i, j) can be written [12]:

$$\frac{\varepsilon_i}{\Delta t}\left[(1-\gamma^*_{i,j})\left(\rho^*_{i,j}\mathrm{Vol}^*_{i,j}+\mathrm{Vol}^*_{i,j}\left(\frac{\partial\rho}{\partial P}\right)^*_T P'_{i,j}+\rho^*_{i,j}\mathrm{Vol}'_{i,j}\right)-(1-\gamma^n_{i,j})\rho^n_{i,j}\mathrm{Vol}^n_{i,j}\right]+(A_rG_r)^{n+1}_{i,j}-(A_rG_r)^{n+1}_{i-1,j}+(A_zG_z)^{n+1}_{i,j}-(A_zG_z)^{n+1}_{i,j-1}=-\delta_{i,2}\dot{m}^{\mathrm{POOL}}_j, \quad (1)$$

where $\dot{m}^{\mathrm{POOL}}_j$ is the pooling rate of the liquid in cell $(2, j)$ and represents excess liquid pooling into the vapor core. The local volume porosity, ε_i, is given as: (a) in the vapor region, $\varepsilon_i = 1$ for $i = 1$; (b) in the wick region, $\varepsilon_i = \varepsilon$ for $2 \leqslant i \leqslant N_L$; and (c) in the liquid annulus, $\varepsilon_i = 1$ for $i = N_L + 1$. The volumes of the mass cells, $\mathrm{Vol}_{i,j}$, are evaluated explicitly, except those in the wick adjacent to the vapor–wick interface. During the startup from a

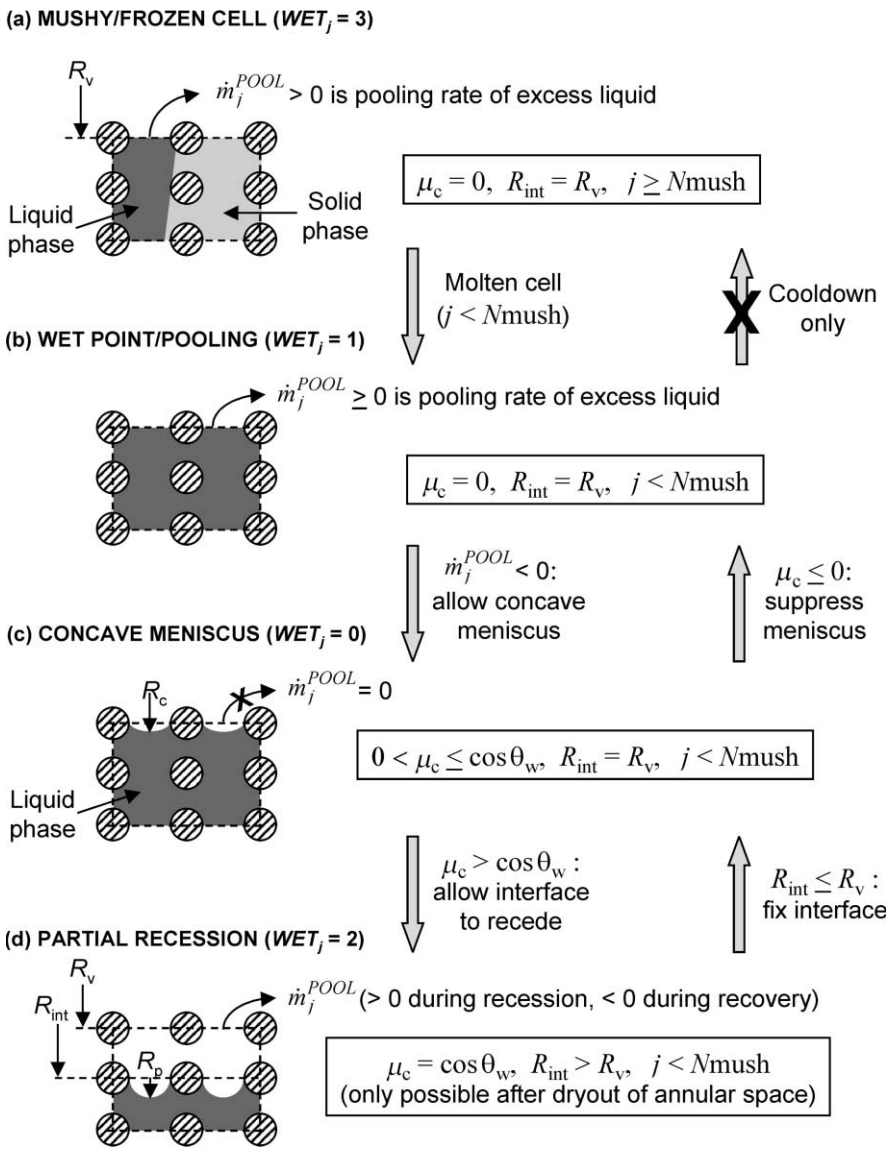

Fig. 2. Illustration of wetting conditions in interfacial wick cells.

frozen state, several interfacial conditions may be present at the wick–vapor interface (Fig. 2), namely: (a) a (partially) frozen or mushy cell; (b) a liquid wet point with a flat liquid–vapor interface; (c) a liquid–vapor interface with a concave liquid meniscus in the surface pores of the wick; and (d) a receding, liquid–vapor interface with a concave liquid meniscus in the surface pores of the saturated wick region. All four occurrences are recognized and accounted for in the numerical solution simulating the startup of the heat pipe from a frozen state. As illustrated in Fig. 2, the volume of the liquid in the vapor–wick interfacial computation cell $(2, j)$ is a function of the radial location of the liquid–vapor interface, R_{int}, the volume fraction of the frozen phase in the voids of the wick, $\gamma_{2,j}$, and the radius of curvature of the liquid meniscus in the surface pores of the wick, R_c. The maximum capillary pressure head developing in the fully-thawed wick occurs when R_c equals the wick's average pore radius, R_p, and the volume of vapor in the hemispherical pores of the wick interfacial computation cell $(2, j)$ is given as

$$V_p^j = \varepsilon\left(\frac{2\pi R_{int}^j \Delta Z_j}{\pi R_p^2}\right)\left(\frac{2}{3}\pi R_p^3\right) = \frac{4}{3}\pi R_p \varepsilon R_{int}^j \Delta Z_j. \quad (2)$$

For the interfacial conditions shown in Fig. 2, when $R_{int}^j \geqslant R_v$, the volume of the liquid phase in the wick interfacial computation cell $(2, j)$ is calculated as

$$\varepsilon(1-\gamma_{2,j})\mathrm{Vol}_{2,j} = (1-\gamma_{2,j})\Big\{\varepsilon\pi\Big((R_\mathrm{v}+\Delta R_2)^2 - (R^j_{\mathrm{int}})^2\Big)\Delta Z_j - \alpha^j_\mathrm{p}V^j_\mathrm{p}\Big\}. \quad (3)$$

Finally, the change in the liquid volume adjacent to the L–V interface is given as

$$\varepsilon(1-\gamma_{2,j})\mathrm{Vol}'_{2,j} = -(1-\gamma_{2,j})V^j_\mathrm{p}(\alpha'_\mathrm{p})_j = -(1-\gamma_{2,j})V^j_\mathrm{p}\left(\frac{\partial\alpha_\mathrm{p}}{\partial\mu_\mathrm{c}}\right)^*_j(\mu'_\mathrm{c})_j. \quad (4)$$

In this equation, the void fraction in the wick interfacial pores, α_p, is a geometrical function of the cosine of contact angle of the liquid meniscus, $\mu_\mathrm{c} = R_\mathrm{p}/R_\mathrm{c}$ [10,12]. The radial momentum jump condition at the liquid–vapor interface relates μ_c to the pressure corrections as [12]:

$$(P^{n+1}_{2,j} - P^{n+1}_{1,j}) + 2\frac{\sigma^\mathrm{L}_j}{R_\mathrm{p}}(\mu^{n+1}_\mathrm{c})_j + \left(\frac{1}{\varepsilon\rho^*_{2,j}} - \frac{1}{\rho^*_{1,j}}\right)(\dot{\bar{m}}^{n+1}_j)^2 = 0. \quad (5)$$

The rates of sublimation, resolidification, and evaporation or condensation at the wick–vapor interface appearing in Eq. (5), are obtained from the kinetic theory of gases, assuming an accommodation coefficient ($a_\mathrm{cc} = 1$) of unity [10,12]:

$$\dot{\bar{m}}_j = a_\mathrm{cc}\left(\frac{M}{2\pi R_\mathrm{g}T^j_{\mathrm{int}}}\right)^{1/2}[P_{1,j} - P_{\mathrm{sat}}(T^j_{\mathrm{int}})] = \Psi(T^j_{\mathrm{int}}, P_{1,j}). \quad (6)$$

After the linearization of the square of the evaporation/condensation rate, the radial momentum balance at the L–V interface in the surface pores of the wick, Eq. (5), is used to relate the corrections μ'_c to the pressure corrections, as

$$2\frac{\sigma^\mathrm{L}_j}{R_\mathrm{p}}(\mu'_\mathrm{c})_j = (P^*_{1,j} - P^*_{2,j}) - 2\frac{\sigma^\mathrm{L}_j}{R_\mathrm{p}}(\mu^*_\mathrm{c})_j + (P'_{1,j} - P'_{2,j}) - \left(\frac{1}{\varepsilon\rho^*_{2,j}} - \frac{1}{\rho^*_{1,j}}\right)\dot{\bar{m}}^*_j\left[\dot{\bar{m}}^*_j + 2\left(\frac{\partial\Psi}{\partial P_\mathrm{V}}\right)^*_j P'_{1,j}\right]. \quad (7)$$

The radial and axial mass fluxes appearing in the mass balance Eq. (1) are expressed in terms of pressures, by discretizing the momentum conservation equations using a staggered grid, and eliminating the off-diagonal velocity corrections using the SIMPLEC (SIMPLE-Consistent) procedure of van Doormaal and Raithby [15], assuming that the off-diagonal corrections are equal to the diagonal corrections. This is a consistent approximation of the momentum correction equations, which does not require any pressure under-relaxation. It was then possible to express all mass flux corrections, advanced-time volumes and densities in terms of pressure corrections. Substituting Eqs. (4) and (7) into the mass balance Eq. (1) gives the following Poisson equation:

$$aP_{i,j}P'_{i,j} + aE_{i,j}P'_{i+1,j} + aW_{i,j}P'_{i-1,j} + aN_{i,j}P'_{i,j+1} + aS_{i,j}P'_{i,j-1} = S_{i,j} - \delta_{i,2}\dot{m}^{\mathrm{POOL}}_j. \quad (8)$$

Eq. (8) are solved for the pressure corrections using a direct, banded Gauss-elimination solver (with normalization and partial pivoting). Since the evaporation/condensation rate corrections are functions of the vapor pressure corrections only (see Eq. (6)), and the vapor volume in the surface pores of the porous wick is calculated explicitly ($\mathrm{Vol}'_{1,j} = 0$), the Poisson equations in the vapor and liquid regions are decoupled ($aE_{1,j} = 0$). This condition increases the stability of the numerical solution and reduces the amount of CPU time, particularly when internal iterations are needed for the convergence of the pooling mass rates, $\dot{m}^{\mathrm{POOL}}_j$.

The numerical solution proceeds by first solving Eq. (8) in the vapor region ($i = 1$, and $j = 1$ to N_z) for the vapor pressure corrections. Then, the evaporation/condensation rates are calculated using Eq. (6). At this point, Eq. (8) is discretized in the liquid/wick region ($i = 2$ to $N_\mathrm{L} + 1$, and $j = 1$ to N_z). In the mass balance equations for the liquid computation cells adjacent to the vapor–wick interface ($i = 2$), the vapor pressure corrections are known and treated explicitly.

The numerical solution accounts for the various occurrences at the wick–vapor interface (Fig. 2). The flag WET_j is introduced to track these different occurrences. Initially, the working fluid in the wick and the annular gap is frozen, all flags are set to 3, and the vapor–wick interface is assumed flat ($\mu_\mathrm{c} = 0$). At some time during the startup transient, as heat is supplied to the evaporator section, the thaw front at the end of the evaporator reaches the vapor–wick interface, allowing the excess liquid in the evaporator to pool into the vapor core (Fig. 2(a)). Since the cosine of the contact angle of the liquid–vapor interface is known at this location ($\mu^{n+1}_\mathrm{c} = \mu^*_\mathrm{c} + \mu'_\mathrm{c} = 0$), the radial momentum jump condition Eq. (7) is solved for the liquid pressure in the computation cell $(2, j)$, in place of the mass balance Eq. (8). Once the Poisson system of equs. has been solved for the pressures in the liquid/wick region, the pooling rate of excess liquid, $\dot{m}^{\mathrm{POOL}}_j$ is calculated using the mass balance Eq. (8) for the computation cell $(2, j)$.

The progression of the thaw front is tracked by the solution of the enthalpy balance equation in the wick [10]. Once the wick's interfacial computation cell is fully-thawed ($\gamma_{2,j} = 0$), the flag WET_j at that location is set to 1 (Fig. 2(b)). As the thaw process progresses towards the end of the condenser, the location of the mushy interfacial computation cell $j = N_{\mathrm{mush}}$ (the cell closest to the condenser end for which $\gamma_{2,j} > 0$) and the accumulation

of excess liquid in the vapor core are tracked. At some time during the startup transient, the calculated pooling rate $\dot{m}_j^{\mathrm{POOL}}$ at a wet point $(2,j)$ may become negative; a situation which arises when the sum of the evaporation rate and of the net liquid flow rate out of the computation cell is greater than the thermal expansion rate of the liquid in the cell. In this case, both the flag WET_j at that location and the pooling rate are set to zero, and the curvature of the concave liquid meniscus in this cell is calculated (Fig. 2(c)). The mass balance Eq. (8) is used for the computation cell $(2,j)$ in the Poisson system of equations, which is solved for the pressures in the liquid/wick region. The interfacial cosine of contact angle μ_{c}^j at this location is then obtained from the radial momentum jump condition Eq. (7), and the wick void fraction is calculated.

The model detects if the heat pipe operation becomes capillary limited, when the calculated μ_{c}^j exceeds the cosine of the wetting angle, $\cos\theta_{\mathrm{w}}$ (Fig. 2(d)). In this case, the flag WET_j at that location is set equal to 2, μ_{c}^j is set to its maximum value of $\cos\theta_{\mathrm{w}}$, and the liquid–vapor interface is allowed to recede ($R_{\mathrm{int}}^j > R_{\mathrm{v}}$). The calculated pressures in the liquid/wick region are used to determine the pooling rate $\dot{m}_j^{\mathrm{POOL}}$ using Eq. (8) for the computation cell $(2,j)$. This pooling rate (positive during recession) causes the liquid–vapor interface to recede down the wick, and the new radial location of the interface R_{int}^{n+1} is obtained from the mass balance:

$$\varepsilon\pi\left[\rho_{2,j}^{*}(R_{\mathrm{int}}^{n+1})_j^2 - \rho_{2,j}^{n}(R_{\mathrm{int}}^{n})_j^2\right]\Delta Z_j = \dot{m}_j^{\mathrm{POOL}}\Delta t. \tag{9}$$

3.2. Liquid pool in vapor core of heat pipe

During the startup transient of the heat pipe from a frozen state, the liquid pool in the vapor core could span the length of the heat pipe between the first wet point $j = N_{\mathrm{wet}}$ (the wick interfacial computation cell $(2,j)$ closest to the evaporator end for which $\mathrm{WET}_j = 1$) and the thaw front in the mushy cell, $j = N_{\mathrm{mush}}$. The accumulated liquid mass in the pool is calculated as

$$M_{\mathrm{POOL}}^{n+1} = M_{\mathrm{POOL}}^{n} + \sum_{j=N_{\mathrm{wet}}}^{N_{\mathrm{mush}}} (\dot{m}_j^{\mathrm{POOL}})^{*}\,\Delta t. \tag{10}$$

The pool is assumed to have a uniform cross-section along the horizontal heat pipe and the liquid in the pool is locally in thermal equilibrium with the heat pipe wick, at T_{int}^j. Once the melting front reaches the end of the condenser ($N_{\mathrm{mush}} = N_z$), all excess liquid in the vapor region is assumed to be sucked by surface tension to accumulate at the end of the condenser, together with the excess liquid from the liquid annulus, forming a liquid plug. The length of such a liquid plug is then calculated based on the mass of liquid pool, its average density, and the vapor core cross-section area. The formation of the liquid plug is done progressively in the present calculations, to avoid numerical instabilities caused by the dramatic change in the mass relocation at the end of the condenser. The thermal model accounts for the thermal energy storage and axial and radial heat conduction in the liquid pool and in the metal plug at the condenser end, and for the heat losses from the latter by radiation to the surroundings.

3.3. Radiative energy exchange between pipe wall, quartz tube and room

As shown in Fig. 1, the Li/Mo heat pipe in the experiment was inserted coaxially in a clear quartz (SiO_2 crystal) tube. The annular space in between the heat pipe and the quartz tube was evacuated to eliminate heat losses by convection or conduction. The 30-cm-long induction coil heating the evaporator section was wound on the outside of the quartz tube with its bottom 3 cm above the end of the evaporator section. Because of the high temperature of the heat pipe wall, the entire heat pipe exchanges heat by radiation with the quartz tube and the surroundings. Such radiation exchange is treated herein in an effort to accurately determine the power input to the evaporator section in the experiment. In the present calculations, the heat pipe wall is divided into a number of cylindrical shells ($k = 1$ to N) with gray-diffuse (opaque) surfaces. The quartz tube inner surface, denoted $k = 0$, is assumed isothermal at T_0 and the reflectance of the quartz tube is neglected. The radiation exchange in the cavity, formulated using the net radiation method [16], is illustrated in Fig. 3(a). Considering the kth shell of the wall, having a surface area A_k, its net radiant energy loss is the difference between the radiant heat emitted ($\varepsilon_k\sigma T_k^4$) and the net radiant heat absorbed, $\varepsilon_k q_0^{\mathrm{out}}$ [16]. The outgoing radiant flux from the quartz tube to the heat pipe wall, q_0^{out}, is the sum of the radiant energy emitted by the quartz, the background energy transmitted inward, and the radiant energy reflected by the quartz, which is neglected herein (Fig. 3(a)). Therefore, the net radiant energy loss for A_k can be expressed as

$$\begin{aligned} Q_k^{\mathrm{loss}} &= A_k\varepsilon_k(\sigma T_k^4 - q_0^{\mathrm{out}}) \\ &= A_k\varepsilon_k(\sigma T_k^4 - \bar{\varepsilon}_0\sigma T_0^4 - \bar{\tau}_0\varepsilon_{\mathrm{R}}\sigma T_{\mathrm{R}}^4), \quad \text{for } k = 1 \text{ to } N. \end{aligned} \tag{11}$$

The effective radiative properties of the quartz, $\bar{\varepsilon}_0$ and $\bar{\tau}_0$, depend on the spectral emittance ε_λ and transmittance τ_λ. Quartz is transparent to infrared radiation below $\sim$4 μm and opaque above $\sim$6 μm [17]. For simplicity, a two-waveband model (with a cut-off wavelength, $\lambda_{\mathrm{c}} = 4$ μm) is used to describe the radiative properties of the quartz tube (Fig. 3(b)), as follows:

(a) Below λ_{c}, in the transparent band (denoted by a *prime*), the spectral transmittance of quartz is taken

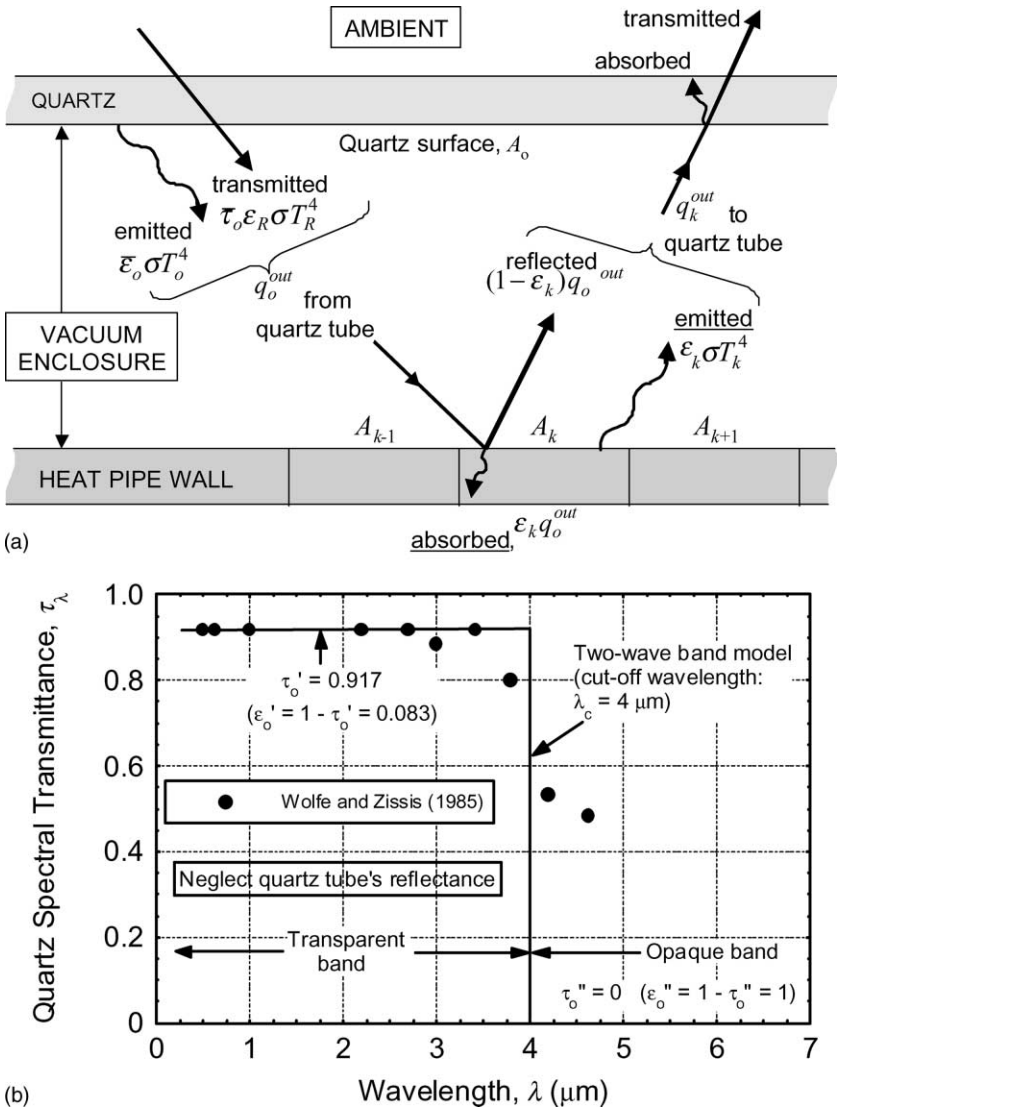

Fig. 3. (a) Illustration of radiant energy exchange in quartz vacuum enclosure. (b) Spectral transmittance of fused quartz—data and model.

constant, $\tau_0' = 0.917$; the spectral reflectance is neglected ($\rho_0' = 0$), and the spectral emittance is thus constant, $\varepsilon_0' = 1 - \tau_0' - \rho_0' = 0.083$;

(b) Above λ_c, in the opaque band (denoted by a *double prime*), the spectral transmittance of quartz is nil; $\tau_0'' = 0$. The spectral reflectance is neglected, $\rho_0'' = 0$, and the spectral emittance equals unity, $\varepsilon_0'' = 1 - \tau_0'' - \rho_0'' = 1$, so that the quartz effectively emits as a black body in this band.

Using this two-waveband approach, the effective radiative properties of the quartz tube, $\bar{\varepsilon}_0$ and $\bar{\tau}_0$, are expressed as

$$\bar{\varepsilon}_0 = \int_0^{+\infty} \varepsilon_\lambda M_\lambda \,\mathrm{d}\lambda \left(\int_0^{+\infty} M_\lambda \,\mathrm{d}\lambda \right)^{-1} = \tau_0' G'_{\lambda_c T_R}, \quad \text{and} \tag{12a}$$

$$\bar{\tau}_0 = \int_0^{+\infty} \tau_\lambda M_\lambda \,\mathrm{d}\lambda \left(\int_0^{+\infty} M_\lambda \,\mathrm{d}\lambda \right)^{-1} = \varepsilon_0' G'_{\lambda_c T_0} + \varepsilon_0''(1 - G'_{\lambda_c T_0}), \tag{12b}$$

where M_λ is the spectral radiance of the blackbody and $G'_{\lambda_c T}$, the fraction of the total emittance of a blackbody at a temperature T, within the wavelength interval $[0, \lambda_c]$, is a well tabulated function of the product $(\lambda_c T)$:

$$G'_{\lambda_c T} \equiv \int_0^{\lambda_c} M_\lambda \, d\lambda \Big/ \int_0^{+\infty} M_\lambda \, d\lambda = \frac{1}{\sigma} \int_0^{\lambda_c T} \frac{C_1}{e^{C_2/(\lambda T)} - 1} \frac{d(\lambda T)}{(\lambda T)^5} = \Phi(\lambda_c T). \quad (13)$$

Wiebelt [16,18] has proposed the following polynomial series representation of this function:

$$G'_{\lambda_c T} = \frac{15}{\pi^4} \sum_{k=1}^{+\infty} \frac{e^{-k\beta}}{k^4} \{[(k\beta + 3)k\beta + 6]k\beta + 6\}. \quad (14)$$

The dimensionless coefficient, $\beta = C_2/(\lambda_c T) \geqslant 2$. Note that for $\lambda_c = 4$ μm, $\beta \simeq 3600/T$, and Eq. (14) is valid for temperatures as high as ≃1800 K. Using only the first 3 terms of the series, the maximum error was 0.02% for $\lambda_c T = 7200$ μm K ($\beta = 2$). At room temperature (300 K), the normalized spectral radiance, $M_\lambda/(\sigma T^4)$, is essentially nil when $\lambda < 4$ μm, and the quartz tube behaves as an opaque blackbody. As the quartz tube temperature increases, the spectral distribution moves to lower wavelength and becomes sharper. As a result, the quartz tube becomes effectively more transparent at higher temperature. The two-waveband approach becomes especially important as the peak of the spectral radiance approaches the cut-off wavelength λ_c, near about 800 K. Since the quartz tube temperature, T_0 was measured in the experiments, it was easy to express T_0, $\bar{\varepsilon}_0$ and $\bar{\tau}_0$ as functions of time during the startup transient. For the purpose of estimating the radiation exchange between the quartz tube and the surrounding, the latter is modeled as a black body ($\varepsilon_R = 1$) radiating to the room temperature, T_R.

4. Simulation of the startup from a frozen state

The Mo–Li heat pipe weighs 1.757 kg and has a thermal energy storage capacity of 679.5 J/K at 1500 K. The three most massive components of the heat pipe, in a decreasing order, are the Mo wall (1.541 kg), the Mo–41wt.%Re screen wick (134.6 g), and the lithium working fluid (30.0 g). Although the mass of the working fluid is only 22% of that of the screen wick, it has about 4 times the heat storage capacity of the wick, due to the high specific heat capacity of lithium. The hafnium foils contribute only 0.2% to the total thermal energy storage capability of the heat pipe, and can be neglected. The other molybdenum components in the heat pipe, namely the wick plug, evaporator end plug, plug attachment piece, and condenser end cap (in a descending order) weigh a total of 44.1 g, contributing only 2.5% to the total mass of the heat pipe, and have a combined thermal energy storage capability of 14.51 J/K, or 2.1% of that of the heat pipe. Therefore, the effect of these components on the transient, thermal operation of the heat pipe was neglected.

4.1. Estimates of net heat input to the evaporator

Because the evaporator section of the heat pipe in the experiment was inductively heated, the net power input to the evaporator section is not known a priori. The power input to the evaporator section is estimated as a function of time in the experiment based on the wall temperature measurements, after accounting for the radiation heat losses along the condenser section and the rate of thermal energy storage in the various components of the heat pipe and the working fluid. At steady-state, the rate of energy storage in the heat pipe is zero, and the net thermal power input to the evaporator equals that radiated away in the condenser section. The measured wall temperature in the condenser section was fitted numerically at different times during the startup transient, assuming the wall temperature in the evaporator section was uniform and equal to the value measured by the closest wall thermocouple. Then, the thermal energy storage in the heat pipe component was computed accordingly. The evaporator section of the heat pipe was fully-thawed after ~7 min into the startup transient, and the amount of liquid in the heat pipe was calculated assuming a constant thaw rate of 1 cm/min, determined based on the wall thermocouple measurements (Fig. 4) [14].

The predictions of thermal energy storage in the evaporator and condenser sections during the startup transient of the lithium heat pipe, from 293 K to a steady-state temperature of 1540 K, are shown in Fig. 5(a). Their sum was fitted using a polynomial function, and the total energy storage rate in the heat pipe is obtained from the derivative of this function with time (Fig. 5(b)). Fig. 6 presents an illustration of the predicted progression of the thaw front and the transitions in the vapor flow regime during the startup of the heat pipe in the experiments. As indicated in Fig. 5(a), after about 30 min into the transient, the energy stored in the

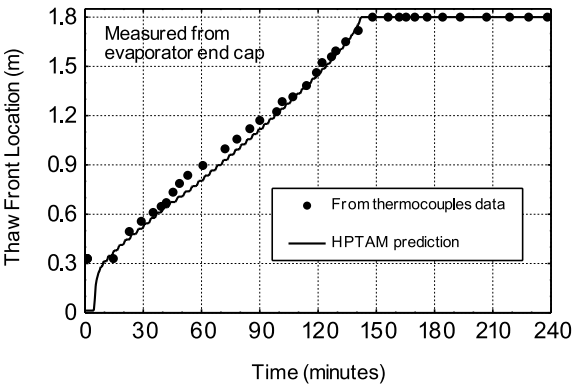

Fig. 4. Comparison of measured and predicted thaw front locations.

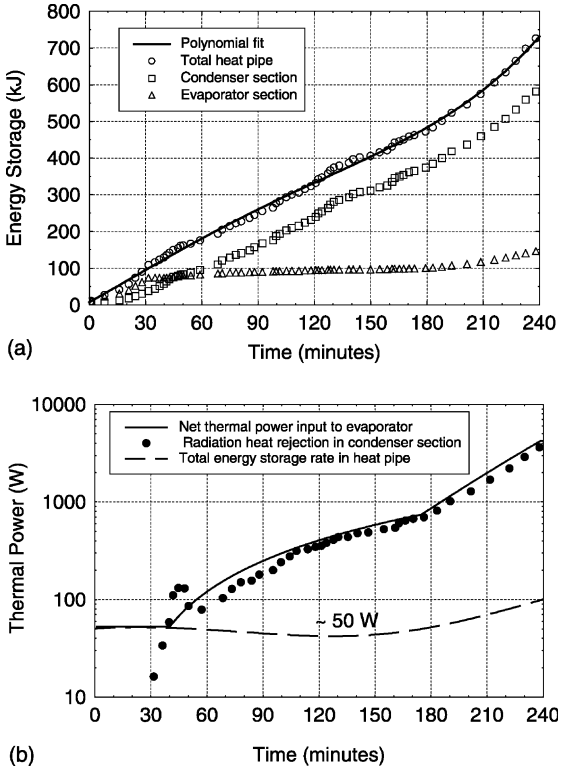

Fig. 5. (a) Estimated energy storage in heat pipe based on temperature measurements. (b) Estimated thermal power input to evaporator based on temperature measurements.

evaporator section is nearly constant and the vapor in the evaporator section is in the transition flow regime, while in the condenser the vapor flow is in the free-molecule regime (Fig. 6(a)). As shown in Fig. 5(b), the estimated rate of the total energy storage in the heat pipe, up to 3 h into the startup transient, is nearly constant at ~50 W. At such time (3 h), the continuum vapor flow front reached the end of the condenser (Fig. 6(d)). The corresponding inflection point in the net evaporator input at this time marks the beginning of the fully-thawed heat pipe operation. After about an hour into the startup transient, the radiation heat losses dominate, with their rate increasing with time as the wall temperature increases (Fig. 5(b)). At earlier times, the contributions of the energy storage and radiation heat losses are comparable (Fig. 5(b)). This figure also shows the calculated input power to the evaporator section, which is the sum of the total thermal energy storage rate and the rate of radiation heat losses from the wall in the condenser section.

4.2. Results and discussion

The present numerical scheme divides the 30-cm-long evaporator section into nine axial computational cells and the condenser section into 47 axial cells, including three axial cells along the Mo condenser end plug. In the radial direction, one computation cell each is used in the vapor core, the wick, and the liquid annulus, and four cells are used in the wall. In this simulation, the lithium mass in the heat pipe is only 29.2 g, since the contribution of the 0.8 g present in the region occupied by the hafnium getter at the evaporator end is neglected (Fig. 1). The simulation of the four-hour startup transient, using a variable time step of 0.125–0.250 s, took about 6 h of CPU time on a 700 MHz AMD-Athlon PC computer. To evaluate the accuracy of the solution, the same startup was simulated using a time step that was 5 times smaller. The predicted wall temperatures in both cases were within ±3 K at all times. Results showed that the radiation heat losses along the condenser section increased steadily up to 3 h into the transient, and the transition vapor flow front moved along the heat pipe, at nearly constant speed (Fig. 6(a)–(c)). During this transient phase, the difference between the evaporator power input and the condenser radiation heat losses is nearly constant at ~50 W, corresponding to the rate of energy storage in the condenser region (Fig. 5(b)). After 3 h into the transient, the continuum vapor flow front reached the end of the condenser (Fig. 6(d)), and the condenser radiation heat rejection rate followed closely the input power to the evaporator, in a quasi-steady state manner. At 240 min, the heat pipe transported 4.0 kW, which corresponds to a power throughput of 2.4 kW/cm^2 and evaporator wall heat flux of 22.2 W/cm^2.

Results confirmed the successful startup of the heat pipe, without ensuing a dryout in either the wick or the liquid annulus in the evaporator section, and reaching a quasi-steady state after ~4 h. At steady-state, the heat rejection in the condenser section was limited by the low emissivity (0.15 at 1500 K) of the polished molybdenum wall. Also, the maximum thermal power to the evaporator in the experiment was limited by the coupling between the evaporator wall and the induction coil.

4.3. Comparison with experimental measurements

The measured and predicted locations of the melting front are compared in Fig. 4. The heat pipe was instrumented with 8 thermocouples along the condenser wall, and the thaw front location was inferred in the experiments by interpolation, from the observed progression of the fusion temperature of lithium along the heat pipe [14]. As shown in Fig. 4, the predictions of the thaw front location are in excellent agreement with the indicated values from the experimental data. The results confirmed that the evaporator was fully-thawed after about 7 min into the startup transient, and the melting front in the condenser progressed at a nearly constant speed of 1.0 cm/min. The heat pipe was

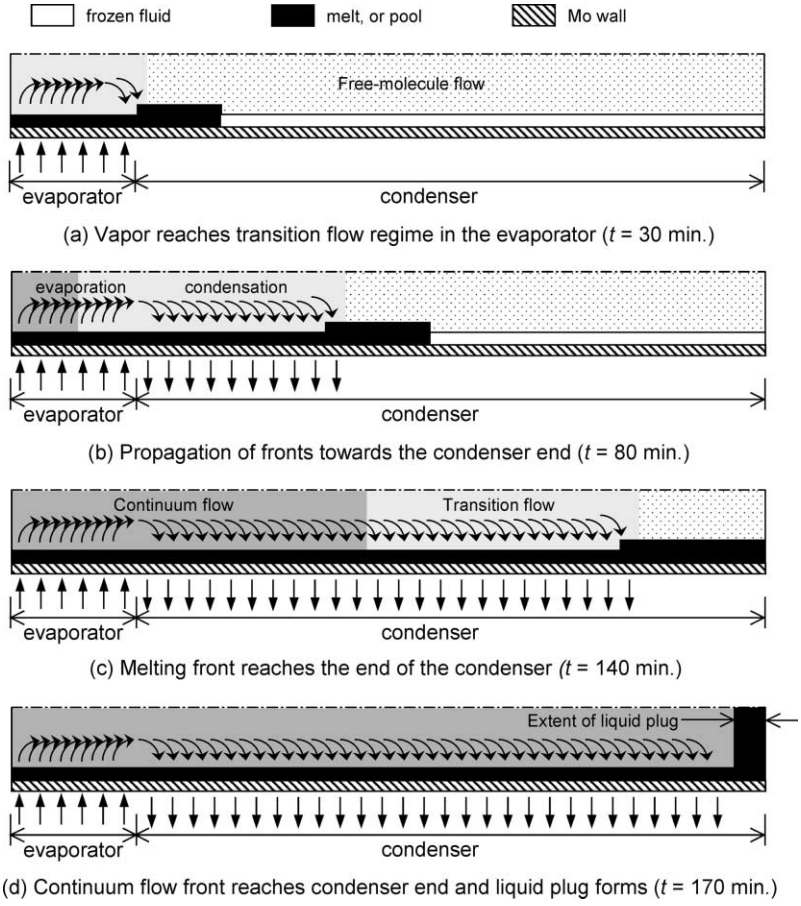

Fig. 6. Illustration of the frozen startup of the lithium heat pipe.

fully-thawed after ~140 min into the startup transient (Figs. 4 and 6(c)).

Fig. 7(a) and (b) compare the measured and predicted wall temperatures, as functions of time and location during the startup transient. The reported uncertainty in the thermocouples measurements is ±20 K [14]. The calculated vapor pressure along the heat pipe, at different times during the startup transient, is shown in Fig. 8. The vapor pressure corresponding to the melting point of lithium (453.7 K) is 0.07 μPa. In Fig. 8, Knudsen numbers of 1.0 (1.9 Pa at $T_{tr}(2) = 820$ K) and 0.01 (269 Pa at $T_{tr}(1) = 1050$ K) indicate the transitions from free-molecule to transition and from transition to continuum vapor flow regimes, respectively, [1,11]. Early in the startup transient, the three vapor flow regimes co-existed in the heat pipe (Figs. 6(b) and (c) and 8). After about 30 min into the transient, the vapor in the evaporator section was in the transition flow regime and the evaporator temperature was nearly uniform and increased very slowly with time (Figs. 7 and 8). The transition vapor flow front traversed the condenser section at a constant speed equal to that of the thaw front (Figs. 6(b) and (c), 7 and 8). Most of the condensation occurred along this transition zone (Fig. 6(b) and (c)), as thermal energy was stored in the pipe wall, wick, and the working fluid, at a rate of ~50 W. These results are characteristic of the frontal startup of alkali-metal heat pipes [11].

4.4. Effect of excess liquid on thermal response of heat pipe

Immediately after the evaporator section was fully-thawed (~7 min into the transient), excess liquid lithium started to pool into the vapor core (Fig. 9), essentially in place, because of the low vapor flow and the low rates of evaporation and re-solidification in the free-molecule regime. The transition vapor flow front, the melting front, and the first wet point at the wick surface all progressed very slowly towards the condenser end, at a near constant speed of about 1 cm/min. The excess liquid pooling into the vapor core at the wet points re-

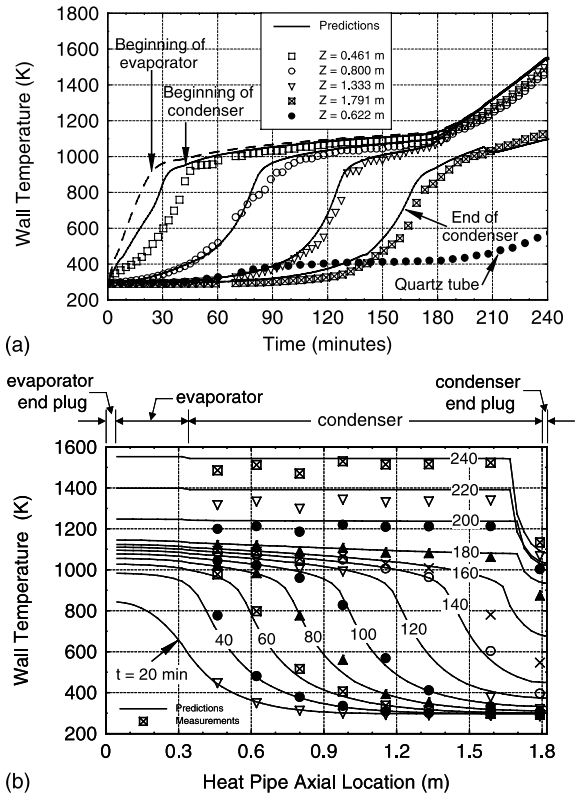

Fig. 7. (a) Comparison of measured and predicted temperatures during startup transient. (b) Heat pipe axial wall temperature distribution during startup.

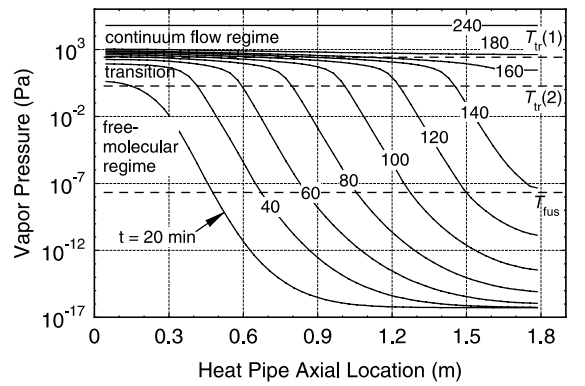

Fig. 8. Predicted vapor pressure in heat pipe vapor core.

mained in place, until it was pushed towards the condenser end by the slow moving high-pressure front of the continuum vapor flow. The liquid in the wick and annulus was no longer stagnant, re-circulating back towards the evaporator, thus participating in the heat pipe operation. As a result, up to 140 min into the transient, the excess liquid in the vapor core spanned the length (20–30 cm) between the first wet point along the heat pipe and the melting front (Figs. 6 and 9(b)). The excess liquid in the vapor core was assumed in thermal equilibrium with the underlying wick. During this phase of the heat pipe startup transient, the average temperature of the excess liquid pool (620 K) remained nearly constant, due to the frontal aspect of the startup transient, while the extent of the pool increased slowly with time, since the thaw front moved slightly faster than the first wet point and the transition vapor flow front (Fig. 9(b)).

Once the thaw front reached the end of the condenser (~140 min), the excess liquid was sucked, by capillary action, to form a liquid plug at the end of the condenser (Figs. 6(b) and 9(d)). However, the formation of the liquid plug is done progressively in the calculations, to avoid numerical instabilities. As shown in Fig. 7(b), the presence of the liquid pool caused a precipitous drop in the wall temperature near the end of the condenser. Normally, during the startup, the location of the continuum vapor flow front marks the interface between active and inactive portions of the condenser. As shown in Fig. 7(a), the predicted and measured wall temperatures at axial location Z_i aligned themselves with the

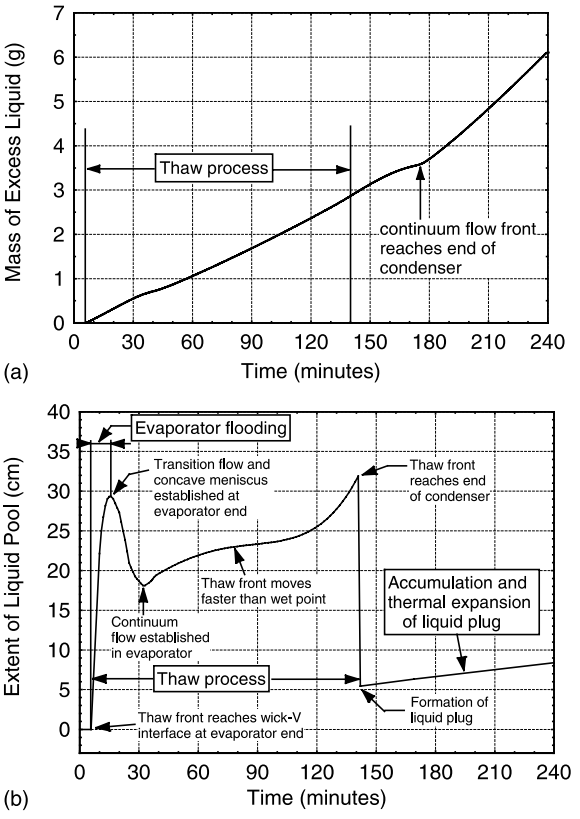

Fig. 9. (a) Predicted mass of excess liquid in vapor core of heat pipe. (b) Predicted extent of excess liquid in vapor core of heat pipe.

evaporator temperature of the heat pipe after the high-pressure front passed this location. However, this re-alignment did not occur at the thermocouple located at the end of the condenser ($Z_i = 1.791$ m). Instead, the wall temperature at that location remained 200–450 K lower than the evaporator temperature, and the wall temperature at the end of the condenser dropped sharply (Fig. 7(b)). Note the small break in the predicted wall temperature at $Z_i = 1.791$ m at 205 min (Fig. 7(a)), which is due to the fixed numerical discretization of the liquid plug. After the liquid plug was formed at the end of the condenser, further accumulation and volume expansion of liquid caused the plug to expand towards the evaporator end (Fig. 9(b)). Once the liquid plug spans another computation cell, it is assumed to fill that cell completely, causing the break in the predicted temperature. This discontinuity could have been eliminated if the liquid plug were modeled with an adaptive numerical grid.

After four hours into the startup transient (240 min), the heat pipe reached quasi-steady state, where the predicted evaporator temperature was 1545 K, compared to 1530 ± 20 K measured in the experiment (Fig. 7(b)). In addition, the predicted wall temperature at the end of the condenser was 1095 K, compared to 1130 ± 20 K measured in the experiment (Fig. 7(b)). The predicted drop in temperature at the end of the condenser was 450 K, compared to 400 ± 40 K measured in the experiment. The precipitous drop in temperature near the condenser end was caused by the presence of the 8.3-cm-long (or 6 g) liquid lithium plug (Figs. 6(d) and 9(a)). The extent of the liquid pool in the experiment was estimated at 9 cm, based on the temperature measurements and visual observations [14]. The calculated pool length was in good agreement with measurements, considering that the contribution to the pool of the 0.8 g in the getter pack region at the end of the evaporator was not included in the modeled inventory of lithium.

5. Summary and conclusions

This work simulated the startup of a horizontal, Li/Mo heat pipe from a frozen state and compared predictions of the time progression of the thaw front and the changes in the wall temperature with time during the startup transient, with reported measurements from an experiment performed at the Los Alamos National Laboratory [14]. In the experiment, the inductively heated heat pipe was placed coaxially inside an evacuated quartz tube and subjected to a ramped power input. The present calculations were performed using the HPTAM computer code after incorporating additional capabilities, which include: (a) tracking the movement of the excess liquid in the vapor core and the eventual accumulation at the end of the condenser; (b) solving the mass, momentum, and energy balance equations in the annular liquid gap between the wick and the heat pipe wall, subject to interfacial boundary conditions with the wick and the wall regions; (c) accounting for the transient, two-dimensional heat conduction in the condenser end plug, which is radiatively cooled on the outside (Fig. 1); and (d) incorporating a two-waveband approximation model to describe the radiation characteristics of the quartz tube surrounding the heat pipe, and calculate the radiative heat losses along the length of the heat pipe, to accurately determine the thermal power input to the evaporator section in the experiment [14].

The predictions of the wall temperature along the heat pipe, at different times during the startup, and of the melting front location, are in good agreement with measurements. The lithium heat pipe started up successfully, without any dryout ensuing in the wick or the liquid annulus in the evaporator section. Due to the very low vapor pressure of lithium, little working fluid mass is lost by sublimation and re-solidification in the frozen section of the condenser during the startup transient. Results also showed that, as the heat pipe reached steady-state operation at an evaporator temperature of 1550 K, the wall temperature near the end of the condenser dropped precipitously by 450 K, due to the formation of a 8.3-cm-long plug of excess liquid at the end of the condenser, and the end heat losses by radiation. After 4 h into the startup transient, the heat pipe was fully-thawed, reaching quasi-steady state, where it transported 4.0 kW. Such thermal power corresponded to a power throughput of 2.4 kW/cm^2 and an evaporator wall heat flux of 22.2 W/cm^2.

Acknowledgements

The authors are grateful to Dr. Robert Reid, of Los Alamos National Laboratory, for his invaluable input on the experiments conduct and results, and for valuable discussions.

References

[1] M.S. El-Genk, J.-M. Tournier, A critical review of free-molecular and transition flow regimes in heat pipes, in: M.A. Merrigan (Ed.), 9th International Heat Pipe Conference, Albuquerque, NM, May 1–5, 1995, Vol. I, Los Alamos National Laboratory, Los Alamos, NM, LA-UR-97-1500, 1995, pp. 497–508.

[2] S.W. Chi, Heat Pipe Theory and Practice: A Sourcebook, Hemisphere Publishing Corporation, Washington, DC, 1976, pp. 121–155, Chapter 5.

[3] R. Ponnappan, L.I. Boehman, E.T. Mahefkey, Diffusion-controlled startup of a gas-loaded liquid-metal heat pipe, AIAA J. Thermophys. 4 (3) (1990) 332–340.

[4] J.H. Jang, A. Faghri, W.S. Chang, E.T. Mahefkey, Mathematical modeling and analysis of heat pipe startup from the frozen state, ASME J. Heat Transfer 112 (1990) 586–594.
[5] Y. Cao, A. Faghri, A numerical analysis of high-temperature heat pipe startup from the frozen state, ASME J. Heat Transfer 115 (1993) 247–254.
[6] Y. Cao, A. Faghri, Simulation of the early startup period of high-temperature heat pipes from the frozen state by a rarefied vapor self-diffusion model, ASME J. Heat Transfer 115 (1993) 239–246.
[7] M.L. Hall, J.M. Doster, A sensitivity study of the effects of evaporation/condensation accommodation coefficients on transient heat pipe modeling, Int. J. Heat Mass Transfer 33 (3) (1990) 465–481.
[8] M.L. Hall, M.A. Merrigan, R.S. Reid, Status report on the THROHPUT transient heat pipe modeling code, in: M.S. El-Genk (Ed.), Proceedings of the 11th Symposium on Space Nuclear Power and Propulsion, Albuquerque, NM, January 9–13, 1994, vol. 2, American Institute of Physics, New York, NY, AIP Conference Proceedings No. 301, 1994, pp. 965-970.
[9] M.A. Merrigan, E.S. Keddy, J.T. Sena, Transient performance investigation of a space power system heat pipe, in: Proceedings of the AIAA/ASME 4th Joint Thermophysics and Heat Transfer Conference, Boston, MA, June 2–4, 1986, American Institute of Aeronautics and Astronautics, Inc., Washington, DC, Paper No. AIAA-86-1273, Los Alamos National Laboratory Report No. LA-UR-86-1567, Los Alamos, NM, 1986.
[10] J.-M. Tournier, M.S. El-Genk, Transient analysis of the startup of a water heat pipe from a frozen state, J. Numer. Heat Transfer, Part A, Appl. 28 (1995) 461–486.
[11] J.-M. Tournier, M.S. El-Genk, A vapor flow model for analysis of liquid-metal heat pipes' startup from a frozen state, Int. J. Heat Mass Transfer 39 (18) (1996) 3767–3780.
[12] J.-M. Tournier, M.S. El-Genk, A segregated solution technique for simulating the transient operation of heat pipes, J. Numer. Heat Transfer, Part B: Fundam. 25 (1994) 331–355.
[13] A. Faghri, M. Buchko, Y. Cao, A study of high temperature heat pipes with multiple heat sources and sinks. Part I: Experimental methodology and frozen startup profiles, ASME J. Heat Transfer 113 (4) (1991) 1003–1009.
[14] R.S. Reid, J.T. Sena, M.A. Merrigan, M.G. Elder, A.L. Martinez, Heat Pipe Development for Advanced Energy Transport Concepts, Phase II—Final Report Covering the Period October 1, 1997, to September 30, 1998, Los Alamos National Laboratory, Progress Report LA-13549-PR, February 1999.
[15] J.P. van Doormaal, G.D. Raithby, Enhancements of the SIMPLE method for predicting incompressible fluid flows, J. Numer. Heat Transfer 7 (1984) 147–163.
[16] R. Siegel, J.R. Howell, Thermal Radiation Heat Transfer, second ed., Hemisphere Publishing Corporation, Washington, DC, 1981, Sections 2–4.11, 5–5, 7–4, 8–3.1 and Appendix A.
[17] W.L. Wolfe, G.J. Zissis, The Infrared Handbook, Environmental Research Institute of Michigan for the Office of Naval Research, Department of the Navy, Washington, DC, 1985.
[18] J.A. Wiebelt, Engineering radiation heat transfer, Holt, Runehart and Winston Inc., New York, NY, 1966.